One-Step Route to Iron Oxide Hollow Nanocuboids by Cluster Condensation: Implementation in Water Remediation Technology

*Lluís Balcells,[a] Carlos Martínez-Boubeta,[*b] José Cisneros-Fernández,[a] Konstantinos Simeonidis,[c] Bernat Bozzo,[a] Judith Oró-Sole,[a] Núria Bagués,[a] Jordi Arbiol,[d] Narcís Mestres,[a] Benjamín Martínez[*a]*

[a] Instituto de Ciencia de Materiales de Barcelona (ICMAB-CSIC), 08193 Bellaterra, Spain.
[b] Freelancer in Santiago de Compostela, Spain.
[c] Department of Physics, Aristotle University of Thessaloniki, 54124 Thessaloniki, Greece.
[d] Institució Catalana de Recerca i EstudisAvancats (ICREA), 08093 Barcelona, Spain.

Corresponding Authors:
*E-mail: benjamin@icmab.es; cboubeta@gmail.com.

ABSTRACT

The fabrication procedure of hollow iron oxide nanoparticles with large surface to volume ratio by a single step gas condensation process at ambient temperature is presented. Fe clusters formed during the sputtering process are progressively transformed into hollow cuboids with oxide shells by the Kirkendall mechanism at the expense of oxygen captured inside the deposition chamber. TEM and Raman spectroscopy techniques point to magnetite as the main component of the nanocuboids, however the magnetic behavior exhibited by the samples suggests the presence of FeO as well. In addition, these particles showed strong stability after several months of exposure to ambient conditions making them of potential interest in diverse technological applications. In particular, these hierarchical hollow particles turned out to be very efficient for both As(III) and As(V) absorption, (326 and 190 mg/g, respectively), thus making then of strong interest for drinking water remediation.

KEYWORDS. Iron oxide magnetic particles; hollow nanocuboids; sputter gas aggregation cluster source; water remediation.

1

Introduction

It is expected that material design in terms of morphology, i.e. increase of the surface to volume ratio, may propitiate substantial advantages for some technological applications in comparison with bare solid particles. For this reason, hollow nanoparticles prepared by taking advantage of the Kirkendall effect, i.e. different interdiffusion rates of atomic species, for instance, cobalt and oxygen, constitutes a very interesting approach.[1] Hollow nanoparticles benefit from an increased (doubled) surface area,[2] which determines their chemical and physical properties, but are also attractive owing to their potential capability of carrying high payloads within the void interior. Therefore, strong interest for determining the real potential applications of these nanoparticles in biomedicine, catalysis, energy storage, etc, exists nowadays.[3,4,5,6] The usual method of fabricating hollow nanoparticles follows a chemical template-based approach.[7] However, template-based methods are expensive and require time-consuming processes of synthesis, which make implementation in large-scale applications complicated. For those reasons, in recent years many efforts have been concentrated into one-pot solvothermal methods or post-oxidation in air at high temperatures.[8,9] However, notable differences exist between products obtained through each route. See for example, the case of cobalt oxide nanoparticles produced in a simple air oxidation process compared with Co_3O_4 hollow nanoparticles obtained from the analogous solution-phase process.[10] In addition, when oxidizing the particles in solution at temperatures above 200 °C, the growth of crystal domains creates large structural strain which, in most of the cases, leads to the fragmentation of the shell and thus compromise long-term stability and practical applications. Therefore, a general approach aimed to define a simple and rational method for fabricating hollow nanoparticles is still lacking.

Besides the strong dependence of the magnetic properties on composition, interfacial effects, shape and size, studies regarding the control of particles' morphology and novel strategies for designing magnetic nanostructures at wish are scarce. For instance, when iron nanoparticles are oxidized a broad range of morphologies, including hollow and core/shell structures[11] are observed. The latter results of special interest due to their particular features because of exchange coupling effects providing opportunities to control the magnetic properties of the bond.[12,13,14] In fact, reports about shape control of nanoparticles obtained by wet synthesis routes are almost reduced exclusively to the case of noble metal nanoparticles such as Ag, Au, Pt. For this reason, physical methods are gaining more and more attention since they allow a better control of the shape and size distribution of nanoparticles.[15] In this sense, gas-phase techniques have undergone remarkable advances in recent years, after Haberland *et al.*[16] developed a nanocluster fabrication system based on magnetron sputtering. This gas aggregation cluster source allows accomplishing a continuous production of particles with a broad range of sizes, while at the same time offers control over chemical composition and structure. A good example of the synthesis of multiple-shell nanoparticles by this method is the work by Huttel et al.[17]Another example is the sputtering and gas aggregation of pure Fe^0 nanoparticles in ultrahigh vacuum conditions and their posterior oxidation under atmospheric pressure in order to obtain non-equilibrium morphologies such as iron-oxide cuboids.[18] Magnetic nanoparticles with a cube-like geometry are of interest because of their potential benefits for enhancing effective magnetic anisotropy, dipolar interactions, packing density and alignment.[19] However, while there are several synthetic procedures to prepare hollow spherical nanoparticles, the methods to prepare cubic shape nanoparticles are scarce.[20]

Herein we present a method to prepare magnetite (Fe_3O_4) hollow nanocuboids with a large surface to volume ratio in a single step process. Their magnetic and structural stability under ambient conditions was checked for a period of 6 months without noticeable degradation. We have also investigated, in particular, their used as adsorbents for capturing of hazardous pollutants in water detecting high specificity to arsenic which allows expecting potential application in drinking water remediation technology.

Experimental Section

Nanoparticles were prepared in a home-built cluster source connected to a vacuum system with base pressure in the low 10^{-6} Torr. A 1 in. diameter DC magnetron with a Fe target (99.95% purity) was operated typically at 100 W. Deposition took place at a nozzle-substrate distance of 25 cm with a constant flux of argon of 65 sccm, and pressures in the low 10^{-3} Torr. Corning glass was used as substrate except for the samples grown for transmission electron microscopy (TEM) imaging, where the nanoparticles were deposited directly on TEM carbon-coated grids, and for arsenic adsorption experiments, where native-oxide terminated silicon substrates were preferred. Immediately after deposition, the samples were removed from the chamber into ambient surroundings. TEM and scanning TEM (STEM) in high angle annular dark field (HAADF) mode were used to study the crystallinity, morphology, size, and dispersion of the samples by means of a Tecnai F20 microscope working at 200 kV. Digital diffraction patterns (DDP) or power spectra were obtained from selected regions in the micrographs. No changes induced by the electron beam were detected in any of the samples.[21]

The Micro-Raman study was done by using a Jobin-Yvon T64000 monochromator with a liquid nitrogen cooled charge-coupled detector. A excitation light line of 514.5 nm from an Ar-ion laser was used. The incident and scattered beams were focused by using an Olympus microscope with

4

a ×50 objective to give a spot size of about 2 μm. Samples consist of few layers of nanoparticles and hence we probed the whole thickness. Due to the polycrystalline nature of the samples unpolarized Raman spectra were taken. An average of ten points was measured on each sample showing a large uniformity over the whole sample surface.

The magnetic properties of percolating thin films were measured using a Quantum Design MPMS-2 SQUID magnetometer in the magnetic field range of ±50 kOe and from 10 to 350 K. Magnetic measurements and TEM analysis were repeated on selected samples to analyze aging effects on magnetic and microstructural properties over a period of 6 months of exposure to ambient conditions. The amount of iron for each sample was measured using an inductively coupled plasma mass spectrometer (ICP-MS) from Agilent (model 7500cx).

To investigate the arsenic adsorption performance of percolating samples on Si substrates, they were submerged in 20 mL of As(III) or As(V) solution; to this end solutions $NaAsO_2$ and $Na_2HAsO_4 \cdot 7H_2O$ in distilled water were prepared. The contact time was approximately 1 h, the concentration used was 10 mg/L, and HCl was added to adjust the pH value at 6. X-ray photoelectron spectroscopy (XPS) spectra were performed with a Phoibos 150 analyzer (SPECS GmbH, Berlin) in ultra-high vacuum conditions (base pressure 1×10^{-10} mbar) using a monochromatic aluminum K-alpha X-ray source (1486.74 eV). The calibration of energies was done by using the C1s peak at 284.8eV, associated to adventitious carbon. The energy resolution, of about 0.58 eV, was determined by measuring the FWHM of the Ag $3d_{5/2}$ peak using a sputtered silver foil.

Results and Discussion

5

The nanoparticles used in this work were prepared by the combination of gas–aggregation technique and magnetron sputtering. Sputtered Fe atoms are cooled down in the cluster source and then aggregate by collisions with flowing Ar gas. Differential pumping drags the clusters through a small nozzle into the deposition chamber. Clusters are finally softly deposited onto a sample holder at room temperature, thus presumably retaining their original shape. In principle, mean nanoparticles' size can be controlled by a careful selection of the deposition conditions (sputtering power, the travelling distances, the chamber pressure and the Ar gas flow rates).[17] Previous reports showed that a oxygen-rich atmosphere into the deposition chamber during processing leads to the formation of Fe/Fe oxide core/shell clusters.[22] Quite differently in our case, the oxygen partial pressure (medium vacuum conditions) in addition to the Ar atmosphere warrants reactive sputtering, thus a chemical reaction occurs leading to the formation of iron oxide shells before clusters were deposited on the substrate. Figure 1A shows a typical HAADF STEM micrograph of as-prepared sample making evident the formation of cuboid-like nanoparticles.
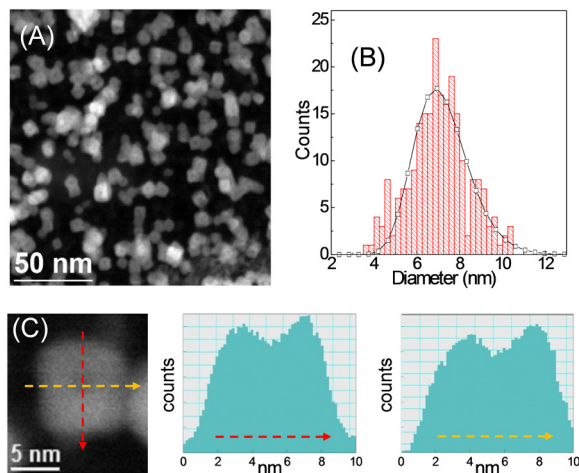
Figure 1. Size distribution and particle morphology. (A) HAADF STEM picture of the Fe particles deposited on a carbon-coated copper grid. (B) Particles sizes histogram. The curve

corresponds to a log-normal probability distribution. (C) Contrast line profile of a nanoparticle revealing the existence of a Kirkendall void in the center of the cuboid.

The HAADF STEM data fit to a log-normal size distribution (Figure 1B) with a mean particle length of 7 nm and 25 % standard deviation, determined by collision statistics and Brownian aggregation in the gas phase.[23] Line profiles (Figure 1C) reveal the presence of a void in the center of a nanoparticle. High resolution TEM (HRTEM) of an individual particles (see Figure 2A) demonstrates the hollow nature of the cuboids, with interior cavities about 2-3 nm surrounded by a ~ 2 nm thick polycrystalline shell. The reflections of the power spectrum pattern (Figure 2B) can be indexed using the cubic spinel structure of Fe_3O_4 (magnetite) and/or γ-Fe_2O_3 (maghemite), it is notoriously difficult to distinguish between them, or an intermediate phase between both.[24] Notice that the indexed reflections correspond to different locations in the nanoparticle, as shown in Figure 2C, where a filtered Fourier transform composition illustrates the polycrystalline nature of the nanocuboid shell.
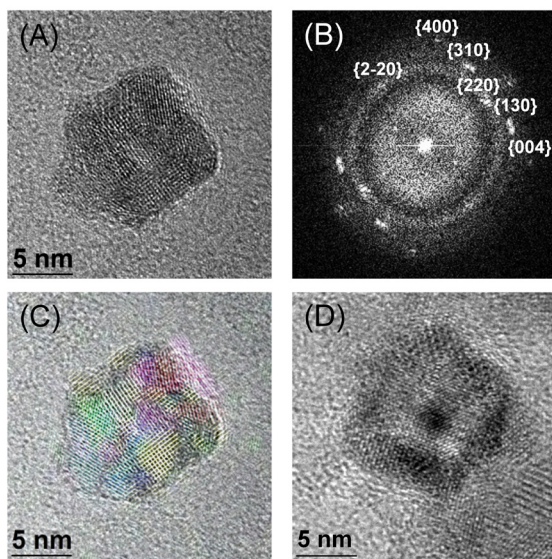
Figure 2. *(A) High-resolution TEM image of a nanocube. The corresponding power spectrum (B) makes evident the plolycrystalline character of the shell. (C) Filtered Fourier transform*

7

composition showing the polycrystalline nature of the nanoparticle cuboid shell, the reflections found in B have been plotted in different colors and superposed to the HRTEM image in A. (D) HRTEM image of a bigger particle with intermediate shape between solid and hollow.

It may be assumed that Fe nanocubes were the seeds where these iron-oxide hollow nanocuboids grown. At this point it is important to note that complete oxidation of cubic Fe nanoparticles seems to promote a change of geometry towards approximately spherical shapes, which is not the case observed here.[18] Even though iron oxidation has been profusely studied in this context in the past, the actual composition of the native oxide is not well established yet. Furthermore, the oxide composition always differs from that corresponding to a stoichiometric bulk oxide.[25] There is also a suggestion that the oxide phase changes depending on the distance from the nanoparticle core.[26] In principle, different oxide compositions can be obtained depending on temperature, oxygen partial pressure and sizes, because the Kirkendall effect is controlled by diffusion.[27] For short timescales, the oxidation process is dominated by the Cabrera-Mott-like mechanism that leads to initial oxidation and the rapid development of about 3 nm-thick oxide shell around the Fe core. Afterward, hollow structures are formed because iron outward diffusion rate through the shell is larger than oxygen inward diffusion, and at the end this process leads to the coalescence of vacancies left behind into a single central void. In fact, it has been previously shown that in the case of Fe nanoparticles at relatively low temperatures (below 250 ºC) there is a critical size above which full reaction with air is not possible, indicating a limiting thickness of ~ 8 nm for which solid particles may be fully converted into hollow oxides.[11] According to this, in the case of large enough nanoparticles, the partial oxidation will promote the formation of core/shell nanostructures with a Fe core trapped inside the oxide shell.[28] It is important to mention here that particles used in this work are just about these sizes. A careful observation allows identifying

8

several particles (about 10 % of the total) that fit quite well with the above suggested growth scheme (i.e., uncompleted oxidation), as shown in Figure 2D where the core is clearly traceable as the darker inner region. The appearance of bridges with the nanoparticle outermost shell and the asymmetric distribution of differentiated contrast regions might well be a result of strain-mediated ionic transport.[18] Similar features has been previously reported for the case of cobalt nanoparticles.[13]

To gain a deeper insight into the growth process and the actual microstructure of the nanoparticles we have also analyzed the role of aging processes. Since TEM and electron diffraction techniques alone cannot give a detailed picture of different oxide phases we have also used Raman spectroscopy, since different bands in the Raman spectrum correspond directly to specific frequency vibration modes that could be very helpful to identify particular oxide phases. In particular, maghemite differs from magnetite in that it contains no divalent iron species. Due to the fact that the ionic radius of Fe (II) is larger than that of Fe (III), Fe (II)-O bonds are longer and weaker than Fe (III)-O bonds; this shifts-up the vibration frequency in the Raman spectrum, and hence Raman analysis allows distinguishing between these phases.
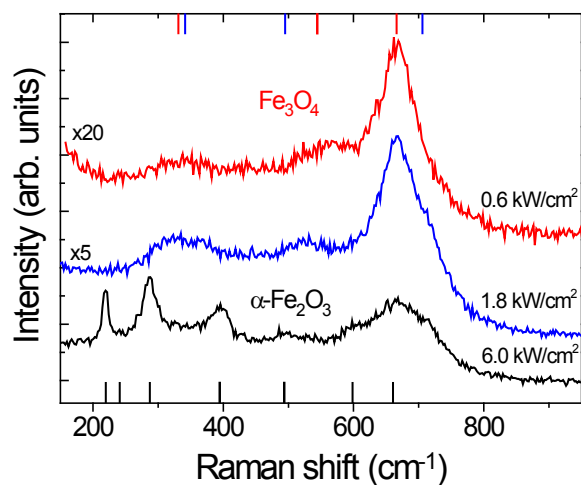

Figure 3. *Raman spectra of the as-grown sample and effect of laser power heating. Scans are vertically shifted for the sake of clarity: top spectrum corresponds to the as-synthesized sample;*

9

increasing laser power density, middle spectrum, shows a mixture of both magnetite and maghemite phases; further increase of laser power heating leads to the transformation into hematite (bottom spectrum). Red, blue and black vertical bars indicate the expected phonon mode frequencies for magnetite, maghemite and hematite nanoparticles respectively, according to Ref. 29.

Raman spectra of samples at different stages of nanostructural transformation are depicted in Figure 3. To avoid sample degradation due to laser heating during observation the laser-beam power density was set to 0.6 kW/cm^2. This fact was carefully checked through successive scans. The Raman spectrum of the as-prepared sample is shown in the upper part. The main features of the spectrum are two bands, a main band centered at 668 cm^{-1} and a secondary one with peaks at ca. 545 and 330 cm^{-1}, that have been assigned to A_{1g}, T_{2g} and E_g vibrational modes of magnetite, respectively.[29] Increasing three times the laser power density, to 1.8 kW/cm^2, promotes local heating of the sample and, as a result of it, bands are shifted to lower wavenumbers and become broader.[30] In addition, a shoulder at ~710 cm^{-1} appears, indicating the formation of maghemite. Maghemite is a metastable phase between magnetite and hematite, and has a very similar crystalline structure to the former. As temperature increases phase transitions proceed as indicated: $Fe_3O_4 \rightarrow \gamma\text{-}Fe_2O_3 \rightarrow \alpha\text{-}Fe_2O_3$. Further increase of the laser density (~6 kW/cm^2) causes the appearance of the characteristic bands of hematite (see lower curve in Fig. 3), namely two A_{1g} modes (220 and 491 cm^{-1}), and the E_g modes at 285, 397 and 597 cm^{-1}. Thus, clearly indicating that $\alpha\text{-}Fe_2O_3$ nucleates after a maghemite-like phase has been formed from magnetite. It is also observed that those changes of spectrum are irreversible.

On the basis of these observations, it is reasonable to assume that the as-synthesized hollows are made of Fe_3O_4. However, some of the observed magnetite bands are very close to those of the non-stoichiometric iron oxide known as wüstite (FeO). In fact, Raman spectrum of FeO is very

10

similar to that of magnetite,[30] with only a small shift in the main peak position. Eventhough Wüstite is unstable at room temperature in bulk form it could be stabilized by surface energy contributions at the nanometric scale. In addition, wüstite also shows small lattice mismatch (~ 3%) respect to the spinel lattice. The presence of Fe_3O_4 along with FeO has been previously reported.[31,32,33] It is reasonable to consider that the oxidation is progressive (in fact, we stress that particular attention should be paid to evidences regarding the non-porous nature of the oxide shell and the impenetrability by gases and liquids neither during the synthesis nor post-preparative procedures),[34] therefore, the higher oxidation states would be present at the outer regions of the hollow shell whereas the wüstite-like phase would be confined to the interior surface. Alternatively, a shell structure based on magnetite but with octahedral vacancies would also be likely,[35] and therefore would show no indication whatsoever for the presence of Verwey transition (T_V) at 120 K.[36] Then, a next plausible possibility which requires further exploration is our samples consist of a mixture of the type Fe_3O_4-FeO, instead of single-phase nonstoichiometric magnetite. Aging effects on the magnetic properties were studied by
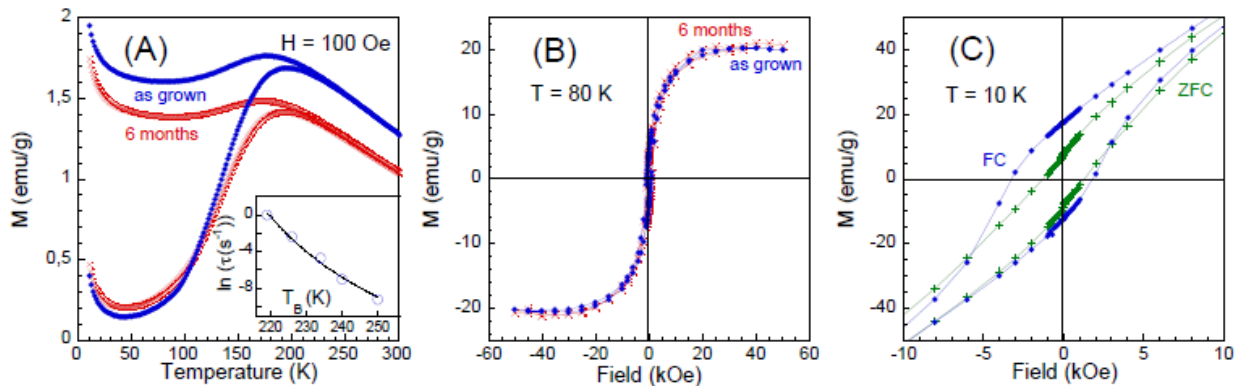
measuring hysteresis loops and thermal dependence of the magnetization after following a zero-field cooling-field cooling (ZFC-FC) process (see Figure 4) after exposure to ambient atmosphere for several months. Similar results to that of as-prepared samples were obtained thus, making evident the stability of the hollow nanoparticles.

11

Figure 4. *(A) Field-cooling and zero-field-cooling (FC-ZFC) magnetization measured with an applied magnetic field of 100 Oe. Similar results were obtained after a long lasting (six months) exposure to ambient conditions. Inset: Blocking temperature dependence on the characteristic relaxation time determined from ac susceptibility measurements. (B) Normalized hysteresis curves at 10 K after ZFC (red) and FC (blue) from 300 K. (C) Shift of the hysteresis loop after a FC process making evident the existence of an exchange bias field.*

As expected, the system exhibits superparamagnetic behavior with a blocking temperature (T_B) around 190 K. The blocking mechanism originates from the competition between thermal energy (which amounts $k_B T$ where k_B is the Boltzmann constant), magnetic anisotropy energy E (proportional to $K_{eff}V$, the effective anisotropy times the mean particle volume), and inter-particles interaction. Obviously, a particle size distribution like that depicted in Figure 1B will result in a blocking temperatures distribution given place to a broad peak in the ZFC curve, as shown in Figure 4A. Though, the estimated T_B is higher than the one anticipated from the effective magnetic volume of the hollows (i.e. the shells) and the usual K_{eff} for iron oxides.[19] The latter is directly probed by temperature-dependent ac susceptibility measurements (see inset in Figure 4A). As pointed out by Néel, the relaxation of the magnetic moment of a single-domain magnetic particle takes place through a thermally activated process according to the Arrhenius law, i.e. $\tau = \tau_0 \exp(E/k_B T)$, being τ the relaxation time and τ_0 the atomic time scale characteristic of the system (typically ~10^{-9} s). It implies that the blocking temperature of the system depends on the observation time window, i.e. measuring the magnetization as a function of the temperature at a given frequency is equivalent to measure it as a function of the field frequency at a fixed temperature. It is important to mention here that, even the generalized Arrhenius law has been extensively used to describe relaxation processes in many materials, the meaningless physical values of τ_0 (~ 10^{-25} s) obtained in this cases indicate that it is not appropriated to describe de magnetic relaxation process of our hollow nanoparticles. It is so because the Néel-Arrhenius model strictly considers a system of single-domain non-interacting identical particles

with their magnetization axes parallel to the applied magnetic field. However, the hollow iron oxide nanostructures described here have a multidomain crystallographic structure (see Figure 2C), which induces a spread of the local anisotropy axes across the shell. Since spins tend to align along the local anisotropy axes, a multidomain magnetic structure is formed within each particle. In addition, magnetic interaction between domains may also become relevant. For instance, competition between exchange terms and anisotropy generates magnetic frustration.[13] Magnetic frustration is also generated by dipolar magnetic interactions in a dense assembly of disordered particles with randomly oriented magnetic moments.[37] Therefore, the competition between the different energy terms leads to a rich variety of magnetic configurations far from the simple postulates of single domain non-interacting identical particles of the Néel-Arrhenius model. For those reasons we have analyzed the relaxation processes of the hollow nanoparticles by using a phenomenological description given by the Vogel–Fulcher law, which is often used in the literature to describe the magnetization dynamics of dipole interacting ferrofluids and for many cluster glasses.[38] The effect of the interaction is taken into consideration through a temperature scale T_0 that measures the interaction energy, and the relaxation time diverges at T - T_0, i.e. so that for temperatures above T_0 the thermal energy dominates the interaction energy. This approach provided anisotropy values about 10^6 erg/cm^3 as well as realistic values for the response time τ_0 and an interaction T_0 close to 200 K. This experimental observation indicates: a) the presence of magnetic interactions among crystallites, and b) the anisotropy energy per unit volume is larger than that of solid counterparts. In fact, the estimated values of K_{eff} are very similar to those determined for other non-interacting iron-oxide hollow nanoparticles prepared by Kirkendall effect.[12] This increment of the anisotropy is commonly associated to translational symmetry breaking and the lower atomic coordination of surface atoms. In fact, in particles of a

13

few nanometers in diameter surface anisotropy is the dominant contribution, and it can be associated to the large proportion of spins with lower atomic coordination. In the case of hollow multidomain nanoparticles this effect is further enhanced due to the large amount of spins located at the innermost or outermost surfaces of the shell and at the crystallographic domain's interfaces. Concomitantly, the large disorder in the hollow nanoparticles leads to the reduction in the number of spins aligning with the external field, reflected in a very low saturation magnetization and a high paramagnetic susceptibility at low temperatures (see Figure 4).

Our previous results, obtained by Monte Carlo simulations, clearly show that the high-field behavior is controlled by the spins of the shell,[12] and the polycrystalline nature of the nanoparticles.[13] The model reproduces a shell with a network of randomly oriented strongly interacting crystallographic domains. Thus, the existence of surface spin canting would account for both the reduction of magnetization and the non-saturating behavior of the hysteresis curves even at large applied fields (Figure 4C). We would like to recall that such magnetic frustration can also explain the observed high coercivity and the shift of the hysteresis loop, when cooling the samples in the presence of a magnetic field, in agreement with previous results reported in polycrystalline maghemite hollow nanoparticles.[12] Additionally, in the present case, low temperature hysteresis loop (Figure 4C) recorded after a FC process from room temperature, is broadened as compared to that measured after a ZFC process and exhibits a non-symmetric coercivity enhancement. These features are usually observed when a ferro(i)magnet is in contact with an antiferromagnet. Therefore, an alternative explanation considers the co-existence of antiferromagnetic and ferromagnetic phases, which coincides with the Fe_3O_4-FeO shell structure proposed above. Previous results by Chalasani and Vasudevan[39] make evident the superparamagnetic behavior above 190 K in cubic nanocrystals of ~10 nm in length while the

14

spherical nanocrystals of similar size exhibited a large decrease of T_B. This significant variation of T_B depending on the particle morphology was attributed to the appearance of a exchange bias field (H_{ex}) in particles of cubic morphology, originated by higher trace amounts of wüstite. Actually, as previously reported, this exchange bias coupling allows obtaining control of the superparamagnetic limit of nanoparticles.[40] In this sense, the existence of antiferromagnetic-coupling is also indicated by the decrease of both ZFC and FC branches of the magnetization below T_B on lowering temperature (see Figure 4A). In addition, the FC magnetic moment increases a little from $T_V \approx 120$ K and peaks at about 200 K. The temperature whereby the sudden increase of magnetization takes place coincides with Néel temperature (T_N) of FeO. Thus, the increase of magnetization can be ascribed to the transition from antiferromagnetic ordering to paramagnetic occurring in FeO at T_N. Since the previously estimated value of T_0 is very similar to T_N, we believe that this antiferromagnetic to paramagnetic transition is the origin of the observed time-dependent relaxation. Finally, the increase of the magnetization below 50 K can be simply attributed to the progressive orientation of surfaces/interfaces uncompensated spins in the field direction on lowering temperature. Nevertheless, some anomalies of the magnetic properties of magnetite around 50 K has been reported previously.[41]

Regarding to the potential applications of these nanoparticles, previous works on hollow iron oxides suggest, for instance, that they will be very promising carriers for future biomedical applications. Nevertheless, the interest of hollows for their payload capacity is limited since when particle size approaches the dimensions of the molecular payload, more molecules can be placed on the surface than inside inner volume. In fact, some recent results make evident that preparation of hollow "tanker" nano-carriers smaller than about 100 nm have no sense.[42] On the other hand, due to the non-porous nature and impenetrability by gases and liquids of the oxide

15

shell,[34] the organic materials that can be potentially encapsulated inside the hollow nanoparticles is restricted. Indeed, porosity and permeability of the shell need to be routinely increased by acid etching prior to drug encapsulation.[43] Nowadays, it is not clear why, using the same coating strategy, a hollow system can have a higher payload than a solid nanoparticle of the same core size. A possibility would be the large occupancy of cation vacancies in hollows shells in comparison with that of the solid counterpart.[44] This difference could modify the reaction ability of transition metal oxides.[45] In fact, the enhanced capacity of lithium ion batteries, which make them useful for application in energy storage, is due to the high concentration of cation vacancies in hollow iron oxide nanoparticles.[6]

Nevertheless, the large effective specific surface area of the hollow structures is of strong interest for other applications such as, for instance, catalysis or selective sensing. In particular we have evaluated the efficiency of hollow nanocubes as adsorbent material in a very relevant subject such as remediation of environmental pollutants. In this regard, several toxic metalloid elements, for instance arsenic, can be found ubiquitously throughout the Earth's crust, and these elements are responsible for important human health problems. For these reasons, the preparation of nanostructures that can offer a large effective specific surface area for capturing selectively these toxic metalloid elements is of major relevance. To this end, four tests were performed to check the efficacy of the hollow nanoparticles for the selective capturing of As: one control (silicon substrate without nanoparticles), the particles in distilled water, and two runs with water spiked with As(III) arsenite and As(V) arsenate to evaluate its performance. As shown in Figure 5, the valence state of As is mostly preserved in the adsorbed species. In particular, the peak observed at binding energy 44.0 eV corresponds to the As(III) 3d peak as expected for $NaAsO_2$ or As_2O_3.[46,47] A small percentage of As(V) should not be excluded as a result of oxidation occurring

16

by dissolved oxygen or X-ray exposure. On the other hand, As(V) spectrum confirms a single peak at 45.3 eV indicative of the sole presence of As(V) species.[48]
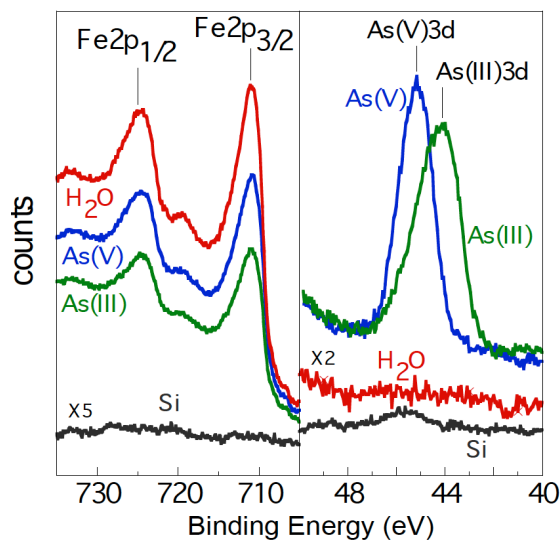
Figure 5. *Effects of sorption of arsenic on the high-resolution XPS spectra at the Fe2p (left) and As3d peak (right). Please note the scale change in the x-axis. Scans are vertically shifted for the sake of clarity: green and blue lines depict the XPS spectra after reaction with either As(III) or As(V). Red line represents the fresh particles in distilled water. The negative controls are performed with the substrate alone (black line). Excluding arsenic, no other chemical constituents changed following the treatment.*

The quantitative analysis of XPS spectra resulted in a As-to-Fe mass ratio which is significantly higher for As(III) (0.326) than As(V) adsorption (0.190). These values imply adsorption capacities of 326 mg/g and 190 mg/g, respectively. A different distribution of As(V) and As(III) species in the present experimental pH conditions may account for the difference in sorption behaviors.[49] As(III) is met in water as a neutral oxy-ion, H_3AsO_3, while As(V) exists mainly as negatively charged forms, i.e. $H_2AsO_4^-$. Therefore, charged As(V) are chemisorbed in a monolayer fashion onto the particles surface while a multilayer coverage by physisorbed oxy-ions is favored for the uncharged As(III). It is to be noted that bidentate binuclear ($R_{As-Fe} \sim 3.3$ Å)

17

and tridentate hexanuclear ($R_{As-Fe} \sim 3.5$ Å) corner-sharing complexes with FeO_6 octahedra were recently described as the exact inner sphere forms corresponding to As(V) and As(III) adsorption on the structure of magnetite.[50] Despite the high initial arsenic concentration used, the results reported here indicate that our hollow nanocuboids clearly have a higher adsorption capacity for arsenic than those previously reported. For instance, estimated adsorption capacity at residual concentration equal to 10 mg/L was found to be around 120 mg/g for As(III) and less than 50 mg/g for As(V) for feroxyhyte powders sieved to mean particle size of 25 μm.[51] Values about 200 mg/g were achieved in hollow iron-cerium alkoxides ~120 nm in size and with the walls thickness about 10 nm.[52] In our case, the unique hollow nanostructure ~7 nm length with a shell thickness about 2 nm can increase the effective specific surface, improving the rate performance. Besides, the hybrid elements (Fe_3O_4 along with FeO) allow, once in water, for an easier exchange between arsenic and the effective sorbent site (α-FeOOH).[53] According to the results above, we can speculate that such systems could be developed as auxiliary devices for water remediation or as sensors for detection and concentration measurements.[54] And although the subsequent dispersion of such particles, from gas aggregation sources in aqueous solutions, is not an easy task, ultrasonication can assist that purpose.[55]

Conclusions

To summarize, we have successfully fabricated hollow magnetic nanoparticles by a single-step physical route using a single precursor. Fe clusters formed during the sputtering process are progressively transformed into hollow cuboids with oxide shells at the expense of oxygen captured inside the deposition chamber by the Kirkendall mechanism. TEM and Raman spectroscopy techniques strongly indicate that magnetite is the main component of the

18

nanocuboids. However the magnetic behavior exhibited by the samples suggests the existence of several oxides in the shell region, with a major contribution from ferrimagnetic Fe_3O_4 andfractions of FeO.

In addition, these particles showed strong stability over several months under ambient conditions, despite many other reports indicating the total or partial formation of maghemite hollows that would, eventually, break into fragments.

Hollow nanocuboids offer a large effective specific surface area that turns out to be very effective for capturing selectively toxic metalloid elements dissolved in water. In particular, when used as adsorbent material for As, these nanocuboids demonstrated a remarkable adsorption capacity for both arsenite and arsenate (above 300 and about 200 mg/g, respectively). Thus, they have the capability to rapidly sequestrate contaminants within minutes from water with a relatively small dose, which would make their application effective and economical.

Overall, the current gas-aggregation fabrication procedure has demonstrated to be of potential interest for the future fabrication of transition-metal oxides particles with hollow interior that can be of strong interest for applications in different fields such as magnetism, catalyst, biomedicine and other. For instance, ternary $CoFe_2O_4$ constructions are believed to exhibit enhanced electrochemical activity with respect to the binary metal oxides Fe_2O_3 and Co_3O_4.[20] We anticipate this could be easily achievable by co-sputtering.

Corresponding Author

*E-mail: benjamin@icmab.es;cboubeta@gmail.com.

19

ACKNOWLEDGMENT

REFERENCES

1. Yin, Y.; Rioux, R.; Erdonmez, C. K.; Hughes, S.; Somorjai, G. A.; Alivisatos, A. P. Formation of Hollow Nanocrystals Through the Nanoscale Kirkendall Effect. *Science* **2004,** *304,* 711–714

2. An, K.; Kwon, S. G.; Park, M.; Na, H. B. Baik, S.-I.; Yu, J. H.; Kim, D.; Son, J. S.; Kim, Y. W.; Song, I. C.; Moon, W. K.; Park, H. M.; Hyeon, T. Synthesis of Uniform Hollow Oxide Nanoparticles through Nanoscale Acid Etching. *Nano Lett.* **2008,** *8,* 4252-4258

3. Shin, J. M.; Anisur, R. M.; Ko, M. K.; Im, G. H.; Lee, J. H.; Lee, I. S. Hollow Manganese Oxide Nanoparticles as Multifunctional Agents for Magnetic Resonance Imaging and Drug Delivery. *Angew. Chem., Int. Ed.* **2009,** *48,* 321−324

4. Xing, R.; Bhirde, A.A.; Wang, S.; Sun, X.; Liu, G.; Hou, Y.; Chen, X. Hollow iron oxide nanoparticles as multidrug resistant drug delivery and imaging vehicles. *Nano Research* **2013,** *6,* 1-9

5. Cheng, K.; Peng, S.; Xu, C.; Sun, S. Porous Hollow Fe3O4 Nanoparticles for Targeted Delivery and Controlled Release of Cisplatin. *J. Am. Chem. Soc.* **2009,** *131,* 10637–10644

6. Koo, B.; Xiong,H.; Slater, m. D.; Prakapenka, V. B.; Balasubramanian, M.; Podsiadlo, P.; Johnson, C. S.; Rajh, T.; Shevchenko, E. V. Hollow Iron Oxide Nanoparticles for Application in Lithium Ion Batteries energy storage. *Nano Lett.* **2012,** *12,* 2429−2435

7.Lou, X. W.; Archer, L. A.; Yang, Z. Hollow Micro-/Nanostructures: Synthesis and Applications. *Adv. Mater.* **2008,** *20,* 3987–4019

8. Peng, S.; Sun, S. Synthesis and Characterization of Monodisperse Hollow Fe3O4 Nanoparticles. *Angew. Chem., Int. Ed.* **2007,** *46,* 4155-4158

9. Guan, N.; Wang, Y.; Sun, D.; Xu, J.A simple one-pot synthesis of single-crystalline magnetite hollow spheres from a single iron precursor. *Nanotechnology* **2009,** *20,* 105603

10. Ha, D.-H.; Moreau, L. M.; Honrao, S.; Hennig, R. G.; Robinson, R. D. The Oxidation of Cobalt Nanoparticles into Kirkendall-Hollowed CoO and Co3O4: The Diffusion Mechanisms and Atomic Structural Transformations. *J. Phys. Chem. C* **2013,** *117,* 14303-14312

11. Cabot, A.; Puntes, V. F.; Shevchenko, E.; Yin, Y.; Balcells, L.; Marcus, M. A.; Hughes, S. M.; Alivisatos, A. P. Vacancy Coalescence during Oxidation of Iron Nanoparticles. *J. Am. Chem. Soc.* **2007,** *129,* 10358-10360

12. Cabot, A.; Alivisatos, A. P.; Puntes, V. F.; Balcells, L.; Iglesias, O.; Labarta, A. Magnetic domains and surface effects in hollow maghemite nanoparticles. *Phys. Rev. B* **2009,** *79,* 094419

13. Simeonidis, K.; Martinez-Boubeta, C.; Iglesias, O.; Cabot, A.; Angelakeris, M.; Mourdikoudis, S.; Tsiaoussis, I.; Delimitis, A.; Dendrinou-Samara, C.; Kalogirou, O. Morphology influence on nanoscale magnetism of Co nanoparticles: Experimental and theoretical aspects of exchange bias. *Phys. Rev. B.* **2011,** *84,* 144430

14. Lima, E. Jr.; ,Vargas, J. M.; Zysler, R. D.; Rechenberg, H. C.; Cohen, R.; Arbiol, J.; Goya, G. F.; Ibarra, A.; Ibarra, M. R. Single-step chemical synthesis of ferrite hollow nanospheres. *Nanotechnology* **2009,** *20,* 045606

15. O'Grady, K.; Bradbury, A. Particle size analysis in ferrofluids. *J. Magn. Magn. Mater.* **1983,** *39,* 91-94

16. Haberland, H.; Karrais, M.; Mall, M.A new type of cluster and cluster ion source. *Zeitschrift für Physik D* **1991,** *20,* 413-415

17. Llamosa, D.; Ruano, M.; Martínez, L.; Mayoral, A.; Román, E.; García-Hernández, M.; Huttel, Y. The Ultimate Step Towards a Tailored Engineering of Core@Shell and Core@Shell@Shell Nanoparticles. *Nanoscale* **2014,** *6,* 13483-13486

18. Pratt, A.; Lari, L.; Hovorka, O.; Shah, A.; Woffinden, C.; Tear, S. P.; Binns, C.; Kröger, R. Enhanced oxidation of nanoparticles through strain-mediated ionic transport. *Nature Mater.* **2014,** *13,* 26–30

19. Martinez-Boubeta, C.; Simeonidis, K.; Makridis, A.; Angelakeris, M.; Iglesias, O.; Guardia, P.; Cabot, A.; Yedra, L.; Estradé, S.; Peiró, F.; Saghi, Z.; Midgley, P. A.; Conde-Leborán, I.; Serantes, D.; Baldomir, D. Learning from nature to improve the heat generation of iron-oxide nanoparticles for magnetic hyperthermia applications. *Sci. Rep.* **2013,** *3,*1652

20. Guo, H.; Li, T.; Chen, W.; Liu, L.; Yang, X.; Wang, Y.; Guo, Y. General design of hollow porous CoFe2O4 nanocubes from metal-organic frameworks with extraordinarily lithium storage. *Nanoscale* **2014,** *6,* 15168-15174

22

21. Herman, D. A. J.; Cheong, S.; Banholzer, M. J.; Tilley, R. D. How hollow structures form from crystalline iron–iron oxide core–shell nanoparticles in the electron beam. *Chem. Commun.* **2013,** *49,* 6203—6205

22. Qiang, Y.; Antony, J.; Sharma, A.; Nutting, J.; Sikes, D.; Meyer, D. Iron/iron oxide core-shell nanoclusters for biomedical applications. *J. Nanopart. Research* **2006,** *8,* 489–496

23. Dekkers, P. J.; Friedlander, S. K. The Self-Preserving Size Distribution Theory. *J. Colloid Interface Sci.* **2002,** 248, 295-305

24. Martıınez-Boubeta, C.; Simeonidis, K.; Angelakeris, M.; Pazos-Pérez, N.; Giersig, M.; Delimitis, A.; Nalbandian, L.; Alexandrakis, V.; Niarchos, D. Critical radius for exchange bias in naturally oxidized Fe nanoparticles. *Phys. Rev. B* **2006,** *74,* 054430

25. Sebastien Couet, Kai Schlage, KarelSaksl, and Ralf Röhlsberger. How Metallic Fe Controls the Composition of its Native Oxide. *Phys. Rev. Lett.* **2008,** *101,* 056101

26. Signorini, L.; Pasquini, L.; Savini, L.; Carboni, R.; Boscherini, F.; Bonetti, E.; Giglia, A.; Pedio, M.; Mahne, N.; Nannarone, S. Size-dependent oxidation in iron/iron oxide core-shell nanoparticles. *Phys. Rev. B* **2003,** *68,* 195423

27. Railsback, J. G.; Johnston-Peck, A. C.; Wang, J.; Tracy, J. B. Size-Dependent NanoscaleKirkendall Effect During the Oxidation of Nickel Nanoparticles. *ACS Nano* **2010,** *4,* 1913–1920

28. Shavel, A.; Rodríguez-González, B.; Spasova, M.; Farle, M.; Liz-Marzán, L. M., Synthesis and Characterization of Iron/Iron Oxide Core/Shell Nanocubes. *Adv. Funct. Mater.* **2007,** *17,* 3870-3876.

29. N. Shebanova, N.; Lazor, P. J. Raman spectroscopic study of magnetite (FeFe2O4): a new assignment for the vibrational spectrum. *J. Solid State Chem.* **2003,** *174, 424-430*

30. de Faria, D. L. A.; Venâncio Silva, S.; de Oliveira, M. T. Raman Microspectroscopy of Some Iron Oxides and Oxyhydroxides. *J. Raman Spectrosc.* **1997,** *28,* 873-878

31. Hai, H. T.; Kura, H.; Takahashi, M.; Ogawa, T. High thermal stability of the ferrimagnetic moment in exchange biased FeO(core)/spinel(shell) nanocubes. *J. Phys.: Conf. Series* **2011,** *266,* 012127

32. Khurshid, H.; Li, W.; Chandra, S.; Phan, M.-H.; Hadjipanayis, G. C.; Mukherjee, P.; Srikanth, H. Mechanism and controlled growth of shape and size variant core/shell FeO/Fe3O4 nanoparticles. *Nanoscale* **2013,** *5,* 7942–7952

33. Lak, A.; Dieckhoff, J.; Ludwig, F.; Scholtyssek, J. M.; Goldmann, O.; Lunsdorf, H.; Eberbeck, D.; Kornowski, A.; Kraken, M.; Litterst, F. J.; Fiege, K.; Mischnick, P.; Schilling, M. Highly stable monodispersePEGylated iron oxide nanoparticle aqueous suspensions: a nontoxic tracer for homogeneous magnetic bioassays. *Nanoscale* **2013,** *5,* 11447−11455

34. Podsiadlo, P.; Kwon, S. G.; Koo, B.; Lee, B.; Prakapenka, V. B.; Dera, P.; Zhuravlev, K. K.; Krylova, G.; Shevchenko, E. V. How "Hollow" Are Hollow Nanoparticles? *J. Am. Chem. Soc.* **2013,** *135,* 2435−2438

35. Toney, M. F.; Davenport, A. J.; Oblonsky, L. J.; Ryan, M. P.; Vitus, C. M. Atomic structure of the passive oxide film formed on iron. *Phys. Rev. Lett.* **1997,** *79,* 4282-4285

36. Santoyo Salazar, J.; Perez, L.; De Abril, O.; Truong Phuoc, L.; Ihiawakrim, D.; Vazquez, M.; Greneche, J.-M.; Begin-Colin, S.; Pourroy, G. Magnetic Iron Oxide Nanoparticles in 1̶0̶40 nm Range: Composition in Terms of Magnetite/Maghemite Ratio and Effect on the Magnetic Properties. *Chem. Mater.* **2011,** *23,* 1379−1386

37. Conde-Leboran, I.; Baldomir, D.; Carlos Martinez-Boubeta, C.; Chubykalo-Fesenko, O.; Morales, M. D. P.; Salas, G.; Cabrera, D.; Camarero, J.; Teran, F. J.; Serantes, D. A Single Picture Explains Diversity of Hyperthermia Response of Magnetic Nanoparticles. *J. Phys. Chem. C* **2015,** *119,* 15698–15706

38. Zhang, J.; Boyd, C.; Luo, W. Two Mechanisms and a Scaling Relation for Dynamics in Ferrofluids. *Phys. Rev. Lett.* **1996,** *77,* 390-393

39. Chalasani, R.; Vasudevan, S. Form, Content, and Magnetism in Iron Oxide Nanocrystals. *J. Phys. Chem. C* **2011,** *115,* 18088–18093

40. Skumryev, V.; Stoyanov, S.; Zhang, Y.; Hadjipanayis, G.; Givord, D.; Nogues, J. Beating the superparamagnetic limit with exchange bias. *Nature* **2003,** *423,* 850-853

41. Hirt, A. M.; Brem, F.; Hanzlik, M.; Faivre, D. Anomalous magnetic properties of brain tissue at low temperature: The 50 K anomaly. *J. Geophys. Res.* **2006,** *111,* B12S06

42. Sailor, M.J. and Park, J.-H. Hybrid Nanoparticles for Detection and Treatment of Cancer. *Adv. Mater.* **2012,** *24,* 3779-3802

43. Cheng, K.; Peng, S.; Xu, C.; Sun, S. Porous Hollow Fe3O4 Nanoparticles for Targeted Delivery and Controlled Release of Cisplatin. *J. Am. Chem. Soc.* **2009,** *131,* 10637–10644

44. Nakamura, R.; Matsubayashi, G.; Tsuchiya, H.; Fujimoto, S.; Nakajima, H. Transition in the nanoporous structure of iron oxides during the oxidation of iron nanoparticles and nanowires. *Acta Mater.* **2009,** *57,* 4261−4266

45. Suntivich, J.; May, K. J.; Gasteiger, H. A.; Goodenough, J. B.; Shao-Horn, Y. A. Perovskite Oxide Optimized for Oxygen Evolution Catalysis from Molecular Orbital Principles. *Science* **2011,** *334,* 1383-1385

46. Wagner, C.D.; Riggs, W.M.; Davis, L.E.; Moulder, J.F.; Muilenberg, G.E. Handbook of X-Ray Photoelectron Spectroscopy, publ. by Perkin-Elmer Corporation, Eden Prairie, MN, **1979**

47. Leonhardt, G.; Berndtsson, A.; Hedman, J.; Klasson, M.; Nilsson, R.; Nordling, C. ESCA studies of some $A_{III}B_v$ compounds with Ga and As. *Phys. Status Solidi.* **1973,** *60,* 241–248

48. Soma, M.; Tanaka, A.; Seyama, H.; Satake, K. Characterization of arsenic in lake sediments by X-ray photoelectron spectroscopy. *Geochim. Cosmochim. Acta.* **1994,** *58,* 2743–2745

49. Tresintsi, S.; Simeonidis, K.; Estradé, S.; Martinez-Boubeta, C.; Vourlias, G.; Pinakidou, F.; Katsikini, M.; Paloura, E.C.; Stavropoulos, G.; Mitrakas, M. Tetravalent manganese feroxyhyte: A novel nanoadsorbent equally selective for As(III) and As(V) removal from drinking water. *Environ. Sci. Technol.* **2013,** *47,* 9699–9705

50. Liu, C.H.; Chuang, Y.H.; Chen, T.Y.; Tian, Y.; Li, H.; Wang, M.K.; Zhang, W. Mechanism of Arsenic Adsorption on Magnetite Nanoparticles from Water: Thermodynamic and Spectroscopic Studies. *Environ. Sci. Technol.* **2015,** *49,* 7726–7734

51. Tresintsi, S.; Mitrakas, M.; Simeonidis, K.; Kostoglou, M. Kinetic modeling of As(III) and As(V) adsorption by a novel tetravalent manganese feroxyhyte. *J. Colloid Interface Sci.* **2015,** *460,* 1–7

52. Chen, B.; Zhu, Z.; Liu, S.; Hong, J.; Ma, J.; Qiu, Y.; Chen, J. Facile Hydrothermal Synthesis of Nanostructured Hollow Iron–Cerium Alkoxides and Their Superior Arsenic Adsorption Performance. *ACS Appl. Mater. Interfaces* **2014,** *6,* 14016–14025

25

53. Amstatter, K.; Borch, T.; Larese-Casanova, P.; Kappler, A. Redox Transformation of Arsenic by Fe(II)-Activated Goethite (α-FeOOH). *Environ. Sci. Technol.* **2010,** *44,* 102–108

54. Haidern, A.F.M.Y.; HedayetUllah, M.; Khan, Z.H.; FirozaKabir; Abedin, K.M. Detection of trace amount of arsenic in groundwater by laser-induced breakdown spectroscopy and adsorption. *Optics & Laser Technology* **2014,** *56,* 299–303

55. Oprea, B.; Martínez, L.; Román, E.; Vanea, E.; Simon, S.; Huttel, Y. Dispersion and Functionalization of Nanoparticles Synthesized by Gas Aggregation Source: Opening New Routes Toward the Fabrication of Nanoparticles for Biomedicine. *Langmuir* **2015,** *31,* 13813-13820